ORIGINAL PAPER

Alessio Roccon

Boiling heat transfer by phase-field method

© The Author(s) 2024

Abstract In this work, we propose and test the validity of a phase-field method tailored specifically for modeling boiling phenomena. The method relies on numerical solutions of the Navier–Stokes equations coupled with a phase-field method and the energy equation. The continuity and Navier–Stokes equations have been modified introducing a source term that accounts for phase change. Likewise, in the conservative Allen–Cahn equation (phase-field method) a source term that accounts for the volume is introduced. The system of governing equations is solved using a projection-correction method and equations are discretized using a second-order finite difference approach. Thanks to the numerical discretization employed, a constant coefficient Poisson equation for pressure is obtained, which can be efficiently solved using FFT-based direct solvers. The proposed method is validated against several benchmarks: an interface undergoing vaporization at a constant rate, the Stefan problem, the adsorption problem, and the growth of a 2D vapor bubble. For all the benchmarks, the present method well matches with analytical and archival literature results for a wide range of vapor-to-liquid density ratios, from $\rho_v/\rho_l = 1$ down to $\rho_v/\rho_l \simeq 5 \times 10^{-4}$ (where ρ_v identifies the vapor density and ρ_l the liquid density).

1 Introduction

Boiling heat transfer represents one of the most effective ways of removing heat and it is commonly used in many engineering applications characterized by large heat fluxes, like nuclear reactors and electronic devices [1–3]. However, the prediction of boiling heat transfer coefficients in these systems still largely relies on empirical correlations, often leading to unsatisfactory results. This is not surprising given the strong multiscale character of the boiling heat transfer process. A wide range of scales is involved in the process, from the molecular scales of the interface that control the nucleation process of vapor bubbles [4–6], to the microscale phenomena that control the micro-layer behavior [7–9], to the larger flow scales that control vapor bubble motion and eventually their breakage and coalescence [10,11].

In this context, numerical simulations play an important role by providing space- and time- resolved information on the flow, interface properties, and temperature in the system. The development of numerical tools for phase-changing flows is very challenging: the wide range of scales involved in the process and their strong coupling requires very refined grids and fast and scalable approaches and eventually the coupling between different approaches [6,9]. Depending on the range of resolved scales, we can distinguish among different methodologies: i) Molecular dynamic (MD) [12–15], where all the nanoscopic scales are resolved

A. Roccon (✉)
Polytechnic Department of Engineering and Architecture, University of Udine, Via delle Scienze, Udine 33100, Italy
E-mail: alessio.roccon@uniud.it

A. Roccon
Institute of Fluid Mechanics and Heat Transfer, TU Wien, Getreidemarkt 9, Vienna 1060, Austria

and thus all the interactions are directly simulated from first principles; ii) Fluctuating hydrodynamics [5,16, 17], a mesoscopic approach that embeds thermal fluctuations, capable of describing spontaneous nucleation phenomena; iii) Interface-resolved simulations, a class of methods where interfacial phenomena that occur at scales comparable to the flow scales are resolved [18–20].

The available numerical approaches for interface-resolved simulations can be classified in two families: interface tracking and interface capturing methods. The fundamental difference resides in the definition of the interface: interface tracking approaches explicitly follow the position of the interface with Lagrangian markers or interface-fitted meshes, while interface capturing methods define the interface position as a prescribed value of a color function or phase-concentration field. Numerical methodologies for boiling phenomena have been proposed for both families. For interface-tracking methods, most of the works rely on the front-tracking technique [21–25] where sets of connected Lagrangian points are used to follow the interface position. Considering interface-capturing methods, numerical approaches have been developed for volume-of-fluid methods [26,27] and level-set methods [28–31]. Recently, phase-field methods have also emerged as a viable tool to simulate phase change phenomena. Specifically, phase-field approaches based on the Cahn-Hilliard equation [32] or the conservative Allen–Cahn equation [10,33–36] have been proposed.

In this work, we propose a a phase-field method (PFM) for boiling heat transfer that relies on the conservative Allen–Cahn (CAC) for the description of the vapor-liquid interface. The PFM is coupled with a direct solution of the mass conservation and Navier–Stokes equation to describe the flow field and the energy equation to describe the temperature field. The continuity and Navier–Stokes equations have been opportunely modified to account for phase change phenomena. The proposed methodology is tailored towards large-scale simulations of phase-changing flows: i) With respect to other methodologies for interface-resolved simulations, present method is interface blind, no geometrical reconstructions are required and thus the computational cost does not depend on the interface topology; ii) From a numerical point of view, the implementation of the phase-field method is relatively simple and efficient; iii) A constant coefficient Poisson equation is obtained for pressure, this allows for the use of fast, scalable and efficient FFT-based direct solvers. Overall, these three aspects enable the future parallelization and porting to GPUs of the method thus allowing for large-scale simulations.

The paper is organized as follows. In Sect. 2, the governing equations and the numerical method are presented. In Sect. 3, the proposed method is validated against benchmarks for phase-changing flows and archival literature data. Then, the proposed method is used to study the growth of a 2D vapor bubble with a constant and uniform vaporization rate. Finally, we draw the conclusions and we discuss future developments in Sect. 4.

2 Methodology

We consider a monocomponent system, composed of its liquid and vapor. To describe the dynamic of the system, we couple direct solutions of the mass conservation and Navier–Stokes equations, used to describe the flow field, with a phase-field method, used to describe the interface position, and the energy equation, used to describe the temperature in the two phases.

2.1 Phase-field method

We employ here a second-order phase-field method for the description of the interface position. The phase-field method relies on a phase-field variable, ϕ, which is constant in the bulk of the two phases ($\phi = 1$ in the vapor and $\phi = 0$ in the liquid) and that undergoes a smooth transition across a thin interfacial layer. The time evolution of the phase field variable is described by the conservative Allen–Cahn equation [37–40], which reads as follows:

$$\frac{\partial \phi}{\partial t} + \nabla \cdot (\mathbf{u}\phi) = \nabla \cdot \left[\gamma \left(\epsilon \nabla \phi - \phi(1-\phi) \frac{\nabla \phi}{|\nabla \phi|} \right) \right] + \frac{\dddot{m}}{\rho_v}, \tag{1}$$

where ϵ is a numerical parameter that controls the characteristic length-scale of the thin transition layer. On the right-hand side, we can distinguish three different terms. The first two terms are the diffusive and sharpening terms, which are also present in the isothermal version of the conservative Allen–Cahn equation [37–39]. These terms allow to preserve the interfacial profile during the computation, e.g. a hyperbolic tangent profile. The strength of these two terms is tuned via the numerical parameter γ, which should be set accordingly so as

to obtain a bounder solution for the phase-field variable [39]. The last term at the right-hand side accounts for the phase change phenomena: $\dddot{m}$ is the vaporization rate per unit volume expressed in kg/m^3s, i.e. the amount of liquid that vaporizes in the unit time and per unit volume, while ρ_v is the vapor density [33,34,41]. The phase change term $\dddot{m}$ is computed from the vaporization rate per unit surface, $\ddot{m}$, expressed in kg/m^2s [32], as follows:

$$\dddot{m} = \ddot{m}|\nabla\phi| = \ddot{m}\frac{\phi(1-\phi)}{\epsilon} \tag{2}$$

where the property of the phase-field variable [37,42] has been used to approximate $|\nabla\phi|$ with a polynomial expression. Specific details on the calculation of the vaporization rate per unit surface are reported in Sect. 2.4.

The main advantage of using the present phase-field method is that by properly selecting the parameters ϵ and γ, it ensures a bounded solution for the phase-field variable [39]. This latter aspect is of great importance when large density ratios are considered and the local value of density (and/or viscosity) is calculated from the phase-field variable [42,43]. In addition, being a second-order partial differential equation, its numerical treatment is easier compared to the Cahn-Hilliard equation where a fourth-order term is present [42,44].

2.2 Hydrodynamics

To describe the flow field, a one-fluid approach is employed and a single set of Navier–Stokes and mass conservation equations is solved in the entire domain [18,20]. For the mass conservation equation, by assuming that the liquid and vapor phases are incompressible, the following equation is obtained [21]:

$$\nabla \cdot (\rho\mathbf{u}) = \dddot{m}\left(1 - \frac{\rho_v}{\rho_l}\right), \tag{3}$$

where ρ_l is the liquid density and ρ_v the vapor density. We can observe that only for the special case $\rho_v = \rho_l$ the flow is divergence-free in the entire domain while, in the most general case where $\rho_v \neq \rho_l$, the divergence-free property is lost in the interfacial region (assuming a non-zero vaporization rate).

The mass conservation equation is coupled with the Navier–Stokes equations to describe the flow field. Using a one-fluid approach, the momentum conservation equations can be written as follows:

$$\frac{\partial(\rho\mathbf{u})}{\partial t} + \nabla \cdot (\rho\mathbf{u}\mathbf{u}) = -\nabla p + \nabla \cdot \left[\mu\left(\nabla\mathbf{u} + \nabla\mathbf{u}^T\right)\right] + \mathbf{f}_\sigma, \tag{4}$$

where ρ and μ are the density and viscosity maps of the domain and $\mathbf{f}_\sigma$ are the surface tension forces. In particular, density and viscosity are defined as linear functions of the phase-field variable [43,45]. The density map is defined as follows:

$$\rho(\phi) = \rho_v\phi + \rho_l(1-\phi), \tag{5}$$

where ρ_v and ρ_l are the vapor and liquid densities. Meanwhile, the viscosity map is defined as:

$$\mu(\phi) = \mu_v\phi + \mu_l(1-\phi), \tag{6}$$

where μ_v and μ_l are the liquid and vapor viscosities. The surface tension forces are evaluated using the localized continuous surface force method [46]. Specifically, the interfacial forces are computed as follows:

$$\mathbf{f}_\sigma = 6\sigma\kappa\phi(1-\phi)\nabla\phi, \tag{7}$$

where σ is the surface tension and κ is the interface curvature, which is defined as follows:

$$\kappa = \nabla \cdot \mathbf{n} = \nabla \cdot \left(\frac{\nabla\phi}{|\nabla\phi|}\right), \tag{8}$$

where $\mathbf{n}$ is the unit normal vector.

2.3 Energy equation

To describe the temperature in the system, the energy equation is solved. By neglecting the viscous dissipation and pressure work due to the incompressibility of the two phases, the temperature in the system can be obtained by solving the following equation:

$$\frac{\partial T}{\partial t} + \nabla \cdot (\mathbf{u}T) = \nabla \cdot (\alpha \nabla T) + S_t \,, \tag{9}$$

where $\alpha = k/\rho C_p$ is the thermal diffusivity and S_t is the source term that accounts for the energy adsorbed/released via the latent heat mechanism. The thermal diffusivity, like density and viscosity, is a function of the phase-field variable:

$$\alpha(\phi) = \alpha_v \phi + \alpha_l (1 - \phi) \,. \tag{10}$$

The source term, S_t, is defined as follows [33,47]:

$$S_t = -\frac{h_{lv}}{C_p} \left(\frac{\partial \phi}{\partial t} + \nabla \cdot (\mathbf{u}\phi) \right) \,, \tag{11}$$

where h_{lv} is the latent heat of vaporization and C_p is the specific heat at constant pressure. In the present work, where boiling phenomena are considered, it can be assumed that one phase (and thus the interface) is always at saturation temperature. This implies that vaporization is driven by one phase solely, i.e. a superheated liquid or vapor. Using this assumption, as the flow field and phase-field carry information related to the latent heat mechanism, the source term S_t can be neglected [34,36,41,48]. Thus, it is sufficient to solve the energy equation only in the superheated phase (the one driving phase change) while the other phase is kept at constant and uniform saturation conditions.

2.4 Calculation of the vaporization rate per unit surface

The last key ingredient required to close the set of governing equations reported above is a closure model for the vaporization rate per unit surface. In archival literature, two different classes of methods are available: energy (or heat conduction) models and kinetic models [32,34,41,49].

The first class of models relies on a balance of the heat fluxes at the interface, i.e. the Rankine-Hugoniot jump condition [29]. Specifically, the net difference between the vapor-to-liquid and liquid-to-vapor heat fluxes at the interface corresponds to the amount of heat absorbed/released at the interface via phase change (i.e. latent heat adsorption/release). The balance of the heat fluxes at the interface can be written as follows:

$$\ddot{m} = q_{v \to l} - q_{l \to v} = \frac{(k_v \nabla T_v - k_l \nabla T_l) \cdot \mathbf{n}}{h_{lv}} \,, \tag{12}$$

where $q_{v \to l}$ and $q_{l \to v}$ are the vapor-to-liquid and liquid-to-vapor heat fluxes, k_v and k_l are the vapor and liquid thermal conductivities, T_v and T_l are the temperatures of the vapor and liquid, h_{lv} is the latent heat of vaporization and $\mathbf{n}$ is the unitary normal vector. This type of model is commonly used in combination with front-tracking [22,23], level-set [50] and phase-field [32,48] methods where accurate information of the interface normal are readily available at run time.

The second class of models relies on the kinetic theory of gases to model mass transfer [51,52]. These models are in general simpler to implement as they do not require the computation of temperature gradients at the two sides of the interface. One of the most commonly used is the model proposed by Tanasawa [53], which contains a linear dependence of the heat flux on the excess temperature of the phase boundary:

$$\ddot{m} = \frac{2\chi}{2 - \chi} \left(\frac{M}{2\pi R_g} \right)^{1/2} \frac{\rho_v h_{lv}(T - T_{sat})}{T_{sat}^{3/2}} \,, \tag{13}$$

where χ is a parameter of the model [49], R_g is the gas constant, M is the molecular weight. This model has been mainly use in combination with volume-of-fluid approaches [27,54,55], although it can be combined with other interface tracking/capturing approaches [56].

In this work, we employ an energy-based model, equation (12), based on evaluating the temperature gradients at the two sides of the interface. The temperature gradients at the vapor and liquid sides are extrapolated using the probe method of Udaykumar et al. [57], which has been mainly applied in the context of front-tracking method [22–24]. In particular, the procedure to compute the vaporization rate per unit surface is composed of the following steps: i) The exact position of the iso-contour $\phi = 0.5$, $\mathbf{x}_i$, is identified using the signed-distance property of the phase-field variable [58]; ii) The temperature gradients at the two probes location, $\mathbf{x}_p = \mathbf{x}_i \pm \Delta \mathbf{n}$, are evaluated, where the distance Δ is set to be of the order of the grid spacing [22,23]; iii) The vaporization rate per unit surface is evaluated and then smeared out in the interfacial layer using equation 2. The present approach resembles the method adopted by Shad and Lee [48] and Haghani-Hassan-Abadi et al. [34] where the vaporization rate is evaluated using a sharp-interface method.

2.5 Numerical method

All the governing equations are solved on a fixed, uniform, staggered grid. Velocity components are defined at cell faces while scalar fields (pressure, phase-field, and temperature) are defined at cell centers. A finite-difference method is used to discretize the equations. Specifically, all spatial derivatives are discretized using a second-order central difference scheme. The time integration of the momentum equation is performed using a first-order projection-correction method [59]. The solution of the phase-field equations and energy equations is time advanced using a first order explicit Euler method.

To advance the solution from the step n to the step $n + 1$, we follow the procedure reported hereunder. The first step is the time advancement of the conservative Allen–Cahn equation to obtain the phase-field variable at the time step $n + 1$. This equation is time advancement using an Euler explicit scheme [39]:

$$\phi^{n+1} = \phi^n + \Delta t A^n \,, \tag{14}$$

where the term A^n includes the advection, diffusion, sharpening and vaporization terms. In particular, the vaporization term is evaluated using the procedure presented in Sect. 2.4. Once obtained ϕ^{n+1}, the density, viscosity and thermal diffusivity maps are evaluated.

The second step is the time advancement of the energy equation, which is performed with an explicit Euler method [21,34,48]:

$$T^{n+1} = T^n + \Delta t B^n \tag{15}$$

where the term B^n includes the advection and diffusion terms of the energy equation. Once known the temperature T^{n+1}, depending on the phase-field value, saturation conditions are imposed on the phase characterized by constant and uniform saturation temperature conditions (i.e. the phase that does not drive phase change). This is equivalent to imposing a saturation Dirichlet boundary condition at the interface.

The final step is the solution of the Navier–Stokes equations, which relies on a first-order projection-correction method [59], opportunely extended to phase change flows [21]. We start by computing the new intermediate field $\mathbf{w}^* = \rho^{n+1} \mathbf{u}^*$ from the following equation:

$$\frac{\mathbf{w}^* - \mathbf{w}}{\Delta t} = C^n \,, \tag{16}$$

where C^n includes the advection, viscous and surface tension terms of the NS equations. Then, by taking the divergence of the following equation:

$$\frac{\mathbf{w}^{n+1} - \mathbf{w}^*}{\Delta t} = -\nabla p \,, \tag{17}$$

where $\mathbf{w}^{n+1}$ is the new velocity field that satisfy the mass conservation equation, we obtain a constant coefficient Poisson equation for pressure:

$$\nabla^2 p = \frac{\nabla \cdot \mathbf{w}^* - \dddot{m}^{n+1}(1 - \rho_v/\rho_l)}{\Delta t} \,, \tag{18}$$

where the second term at the numerator represents the right-hand side of the mass conservation equation. This term is non-zero only in the interfacial regione, where the occurrence of phase change induces a velocity jump.

The main advantage of the present formulation for the NS equations is that FFT-based solvers can be readily applied to solve equation (18). Finally, the correction step is performed to obtain the new field $\mathbf{w}^{n+1}$:

$$\mathbf{w}^{n+1} = \mathbf{w}^* - \Delta t \nabla p \,, \tag{19}$$

and the new velocity field $\mathbf{u}^{n+1}$ is obtained as follows:

$$\mathbf{u}^{n+1} = \frac{\mathbf{w}^{n+1}}{\rho^{n+1}} \,. \tag{20}$$

Once the new velocity field $\mathbf{u}^{n+1}$ is known, all the quantities (velocity, pressure, phase-field and temperature) at the new time step $n + 1$ are available and the solution algorithm is complete.

3 Results

In the following, the proposed phase-field method is validated against benchmarks for phase change problems available in archival literature. First, we consider the vaporization of a flat interface at a constant rate. Second, we consider the Stefan problem, i.e. the phase change driven by a motionless superheated vapor. Third, we analyze the adsorption problem, where phase change is driven by a superheated liquid. Finally, we consider the growth of a two-dimensional vapor bubble.

3.1 Vaporization of a flat interface at a constant rate

The first test case we consider is the vaporization of a flat interface at a constant rate, i.e. a constant value for $\dot{m}$ is assumed. In this problem, a heat flux, q_w, is provided to the left boundary of the domain (wall), as shown in Fig. 1. The left part of the domain is occupied by the liquid while the right part by the vapor. The vapor can flow out from the outlet located at the right side of the domain.

Assuming a slow vaporization rate, the provided heat flux can be considered constant and the interface moves from right to left with a constant velocity V [21,37]. In this scenario, analytical steady-state solutions for the vapor velocity and pressure jump can be obtained. In particular, considering the jump conditions applied at the vapor-liquid interface [37], the velocity in the liquid and vapor phases, u_l and u_v, are:

$$u_l = 0 \,, \qquad u_v = \left(1 - \frac{\rho_l}{\rho_v}\right) V \,, \tag{21}$$

where V is the constant interface velocity (which is negative as the interface moves from right to left); the resulting pressure jump can be computed as:

$$\Delta p = \rho_l \left(\frac{\rho_l}{\rho_v} - 1\right) V^2 \,, \tag{22}$$
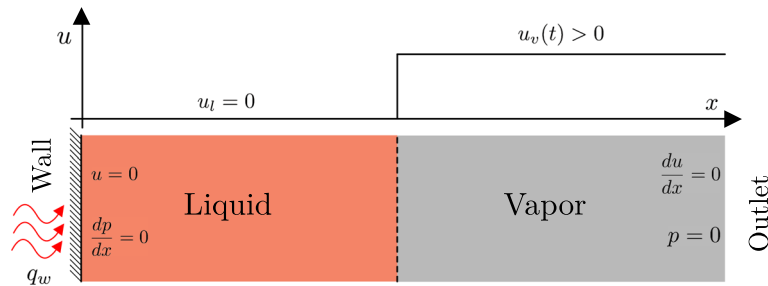

Fig. 1 Graphical sketch of the problem of phase change from a flat interface in the presence of a density difference. The left boundary is a wall where a heat flux, q_w is provided while the right boundary is an outlet where pressure is imposed. The left part is occupied by the liquid phase while the right part by the vapor. The heat flux applied at the wall leads to the vaporization of the liquid phase and the interface moves with a constant velocity, V. The liquid is motionless ($u_l = 0$) while the vapor moves with constant velocity ($u_v(t) > 0$)
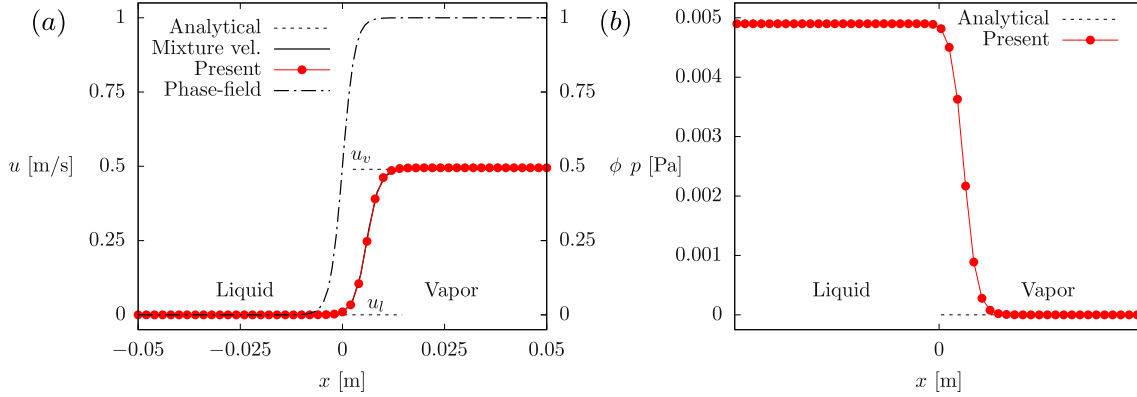
Fig. 2 Behavior of velocity (panel a) and pressure (panel b) for a flat interface undergoing vaporization in presence of a density difference. The liquid phase (left) is motionless while the vapor (right) moves with constant velocity; a pressure jump occurs across the interface due to the phase change. The theoretical values of the liquid and vapor velocity (horizontal dashed lines) as well as the mixture velocity (Eq. 23, black solid line) are reported as reference. The phase-field profile is also shown in panel a with a dot-dashed line (secondary axis on the right). The case shown considers a vapor-to-liquid density ratio equal to $\rho_v/\rho_l = 0.02$

In the context of a one-fluid approach, i.e. when a single set of Navier–Stokes equations is solved in the entire domain, we can introduce the definition of mixture velocity [37]. The resulting mixture velocity in the entire domain (liquid and vapor) can be computed as:

$$u = \frac{\rho_l(1-\phi)u_l + \rho_v\phi u_v}{\rho_l(1-\phi) + \phi\rho_v} = \frac{\rho_v\phi u_v}{\rho_l(1-\phi) + \phi\rho_v} , \tag{23}$$

where ϕ is the value of the phase-field variable ($\phi = 0$ in the liquid and $\phi = 1$ in the vapor); the second expression is obtained by considering that $u_l = 0$.

We can conveniently solve the problem in a moving reference frame that translates with the constant interface velocity [37]. In this new reference frame, the liquid–vapor interface does not move and the phase-field variable remains constant over time (and its transport equation is not solved). We consider two incompressible phases having density $\rho_l = 1\,kg/m^3$ and $\rho_v = 0.02\,kg/m^3$; the resulting density ratio is equal to $\rho_v/\rho_l = 0.02$. The viscosity of the two phases is matched and set equal to $\mu_l = \mu_v = 0.001\,kg/ms$. The interface velocity V is set equal to $0.01\,m/s$. We consider a domain of dimension $L_x = 0.1\,m$ where the interface is located at $x = 0\,m$. At the left boundary (wall), no-slip conditions are applied ($u = 0$) while the right boundary is an outlet where pressure is imposed ($p = 0$). The domain is discretized with $N_x = 100$ grid points and for the phase-field method we set $\epsilon = 1.5\Delta x$.

After a short initial transient, a steady solution is obtained for the Navier–Stokes and mass conservation equations and the resulting velocity and pressure profiles can be compared with the theoretical solutions. Figure 2a shows the numerical velocity profiles compared against the theoretical profile of the liquid, vapor and mixture velocities. As a reference, the phase-field profile is also shown with a dash-dotted line (axis on the right). We observe that the numerical profiles (red dots) are in excellent agreement with the analytical values of the velocity in the two phases (i.e. $u_l = 0\,m/s$ and $u_v = 0.49\,m/s$, black dashed lines). Likewise, the velocity profile matches the analytical behavior of the mixture velocity (black solid line). It is interesting to observe that the mixture velocity profile is not symmetric with respect to the phase-field profile: most of the velocity jump occurs in the region $\phi > 0.5$, in agreement with Sun and Beckermann [37]. Considering the pressure profiles, which are shown in Figure 2b, we notice that the numerical behavior is in agreement with the theoretical behavior (dashed lines). Specifically, pressure exhibits a jump across the interface while it is constant in the bulk of the two phases. The value of the pressure jump is also in agreement with that obtained from Eq. (22), i.e. $\Delta p \simeq 0.049\,Pa$.

3.2 Stefan problem

To test the proposed model with a more challenging problem, we consider the Stefan problem. This problem has been extensively employed in archival literature to perform validation of numerical methods for phase-change problems [26,28,60]. In this problem, an infinitesimally thin layer of vapor is located near the left boundary
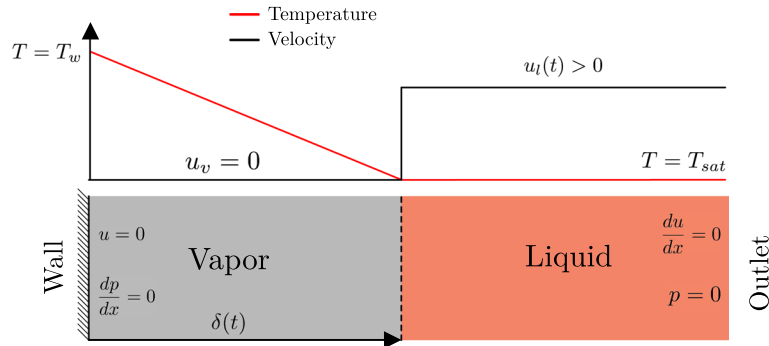
Fig. 3 Graphical sketch of the Stefan problem at a generic time instant $t > 0$. The left boundary is a wall, which temperature is fixed to a value larger than the saturation temperature; the right boundary is an outlet where pressure is imposed. The vapor (left) is superheated while the liquid (right) is at saturation temperature, as shown by temperature profile (red line). At the beginning ($t = 0$), the vapor-liquid interface is initialized at the wall location. The wall superheat drives the vaporization. The vapor is motionless ($u_v = 0$) while the liquid moves with a constant positive velocity ($u_l(t) > 0$). The distance of the interface from the wall, $\delta(t)$, is also highlighted

(wall) while the remainder of the domain is occupied by the liquid phase; the right boundary is an outlet, see Fig. 3. The temperature of the left wall is fixed to a value higher than the saturation temperature, $T_w > T_{sat}$, while the liquid temperature is equal to T_{sat}. The vapor near the wall experiences an increase in temperature and becomes superheated; this drives the vaporization of the liquid. Therefore, the interface moves away from the wall (from left to right) as more liquid is transformed into vapor. In this problem, the vapor is motionless while the volume expansion generated by the vaporization makes the liquid flow from left to right, i.e. towards the outlet (right boundary).

For this problem, an analytical solution is available [23,26,36,60]. Specifically, the interface position, $\delta(t)$, evaluated as the distance of the vapor-liquid interface from the wall, can be calculated from the following equation:

$$\delta(t) = 2\xi \sqrt{\frac{k_v t}{\rho_v C_{p,v}}} = 2\xi \sqrt{\alpha_v t} \,, \tag{24}$$

where k_v is the thermal conductivity and $C_{p,v}$ is the vapor specific heat at constant pressure. In the second expression of the equation reported above, the definition of vapor thermal diffusivity, $\alpha_v = k_v/\rho_v C_{p,v}$ has been introduced. The parameter ξ is obtained via the solution of the following transcendental equation:

$$\xi \exp(\xi^2) \operatorname{erf}(\xi) = \frac{C_{p,v}(T - T_{sat})}{h_{lv}\sqrt{\pi}} \,, \tag{25}$$

where h_{lv} is the latent heat of vaporization. By introducing the Stefan number definition, $St = C_{p,v}(T - T_{sat})/h_{lv}$, the equation above can be rewritten as follows:

$$\xi \exp(\xi^2) \operatorname{erf}(\xi) = \frac{St}{\sqrt{\pi}} \,. \tag{26}$$

Solving this equation for ξ, we obtain the interface position as a function of time. An analytical solution for the temperature distribution in the vapor is also available:

$$T(x, t) = T_w - \frac{T_w - T_{sat}}{\operatorname{erf}(\xi)} \operatorname{erf}\left(\frac{x}{2\sqrt{\alpha_v t}}\right), \tag{27}$$

where T_w is the wall temperature (which is fixed). Finally, once the interface position and vaporization rate are known, from mass conservation, we can also obtain an analytical expression for the velocity in the liquid.

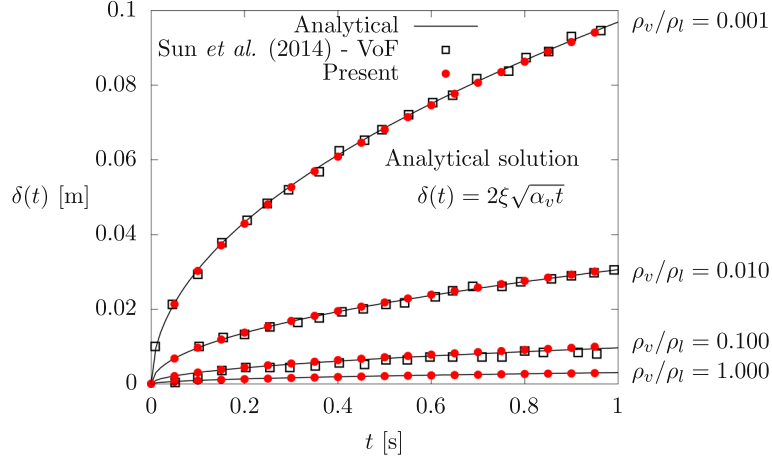$$u_l = \left(1 - \frac{\rho_v}{\rho_l}\right)\xi\sqrt{\frac{\alpha_v}{t}} \,, \tag{28}$$

Fig. 4 Time evolution of the interface position (identified as the iso-contour $\phi = 0.5$) for the Stefan problem. Four different density ratios have been tested: from $\rho_v/\rho_l = 1$ down to $\rho_v/\rho_l = 0.001$. The analytical behavior is reported with continuous black lines (for the four density ratios considered). As the density ratio is decreased, the resulting volume expansion is larger and the vapor pushes the liquid towards the outlet the liquid. The results obtained by Sun et al. [60] using a volume-of-fluid method are also reported as reference using black empty squares

where it is worth noticing that for $\rho_v = \rho_l$, no volume expansion occurs and thus $u_l = u_v = 0$ in the entire domain.

We now numerically investigate the Stefan problem with the proposed method; we employ the setting analyzed by Sun et al. [60] using a volume-of-fluid (VoF) methodology. We consider four different cases, characterized by a different density ratio. In particular, we keep fixed the liquid density equal to $\rho_l = 1 \, kg/m^3$ and we consider four different values of the vapor density: $\rho_v = 1 \, kg/m^3$, $\rho_v = 0.1 \, kg/m^3$, $\rho_v = 0.01 \, kg/m^3$ and $\rho_v = 0.001 \, kg/m^3$, which correspond to a density ratio that ranges from $\rho_v/\rho_l = 1$ down to $\rho_v/\rho_l = 0.001$. The viscosity of the two phases is matched and set equal to $\mu_l = \mu_v = 0.01 \, kg/ms$. The domain has a length equal to $L_x = 0.2 \, m$ and the interface is initially located at $x \simeq 0 \, m$ (for computational reasons, the leftmost cells are initialized as vapor). The domain is discretized with $N_x = 200$ grid points and for the phase-field we set $\epsilon = 1.5\Delta x$, the parameter γ has been set according to Brown et al. [47]. The wall superheat has been set equal to $\Delta T = T_w - T_{sat} = 10 \, K$; the vapor specific heat at constant pressure to $C_{p,v} = 200 \, J/kgK$, the latent heat $h_{lv} = 10^4 \, J/kg$ and the vapor thermal conductivity to $k_v = 0.005 \, W/mK$, thus replicating the values chosen by Sun et al. [60]. The resulting values of the thermal diffusivity range from $\alpha_v = 2.5 \times 10^{-5} \, m^2/s$ (for $\rho_v = 1 \, kg/m^3$) up to $\alpha_v = 2.5 \times 10^{-2} \, m^2/s$ (for $\rho_v = 0.001 \, kg/m^3$). The resulting Stefan number is equal to $St = 0.2$ for all cases and the solution of the transcendental Eq. (26) gives $\xi = 0.3064$.

Figure 4 shows the position of the interface $\delta(t)$ as a function of time for the four different density ratios considered. First, we can observe that as the density is decreased, a larger expansion occurs and the interface travels a larger distance (larger values of δ). This trend can be also observed from the analytical expression of the interface displacement (Eq. 24), as the density is decreased, the thermal diffusivity of the vapor phase increases. Comparing the different cases, we observe an excellent agreement among present results, the analytical profiles and the archival literature data of Sun et al. [60] for the entire range of density ratios considered. Finally, it is worth mentioning that the resulting temperature profiles are almost linear in the vapor phase (and constant in the liquid phase).

We now move to verify the solution of the continuity and Navier–Stokes equations by considering the behavior of the liquid velocity. Results are shown in Fig. 5 for the three unmatched density cases. In general, we can appreciate how the velocity decreases as time advances. This is a direct consequence of the smaller temperature gradient present at the interface (vapor side). Thus, a smaller vaporization rate is attained as the interface moves from left to right (farther from the superheated wall). Comparing the numerical profiles (red dots) and theoretical profiles (black lines), a very good agreement is exhibited for the entire range of density ratios analyzed.
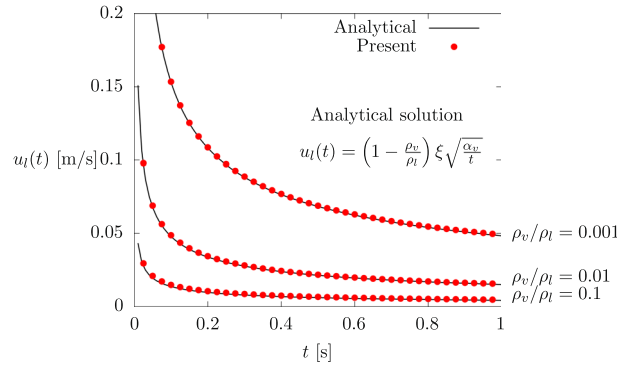
Fig. 5 Time evolution of the velocity in the liquid phase for the Stefan problem. Three different cases are shown: $\rho_v/\rho_l = 0.1$, $\rho_v/\rho_l = 0.01$ and $\rho_v/\rho_l = 0.001$. The case $\rho_v/\rho_l = 1$ is not shown: the two phases have the same density and no expansion occurs during phase change and the velocity is zero in both phases. The analytical behavior is reported with continuous black lines. As the density ratio is decreased, the resulting expansion due to phase change becomes larger and the liquid exhibit larger velocity values
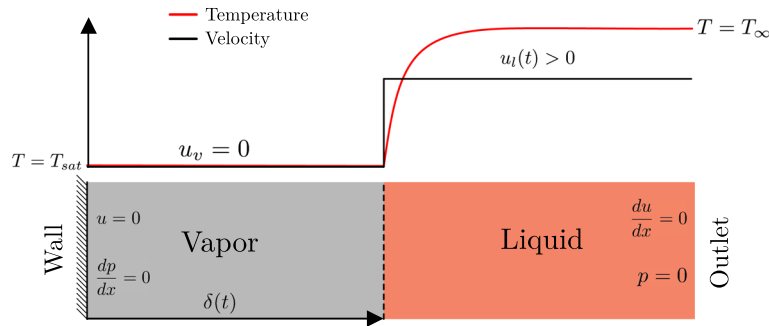
Fig. 6 Graphical sketch of the adsorption problem. The left boundary is a wall, which temperature corresponds to the saturation temperature; the right boundary is an outlet where pressure is imposed. At the beginning, the vapor-liquid interface is located close to the wall. The liquid superheat drives the phase change and as a consequence of the phase change expansion, liquid is driven towards the left boundary. The vapor is motionless ($u_l = 0$) while the liquid moves with constant velocity ($u_l(t) > 0$). The distance of the interface from the wall, $\delta(t)$, is also identified

3.3 Adsorption problem

We consider here the adsorption (or sucking interface) problem. In this problem, the vapor is at saturation temperature, $T_v = T_{sat}$, while the liquid is superheated $T_l = T_\infty > T_{sat}$ and drives the vaporization. A typical temperature profile is shown in Fig. 6. Compared to the Stefan problem, where heat is only transported by diffusion (from the wall to the interface as the vapor is motionless), in this problem, heat is also transported by convection in the liquid [26]. Indeed, the vapor is motionless while the liquid is characterized by a uniform positive velocity. As a consequence, the thermal boundary layer in the liquid is not anymore linear and becomes steeper. Apart from the difference in the driving vaporization mechanism, the behavior of the vapor-liquid interface is qualitatively similar to the one obtained in the Stefan problem: the interface moves away from the wall as more liquid is transformed into vapor.

An analytical solution is available also for the adsorption problem [23, 26, 61–63]. In particular, the interface position can be predicted by the following equation:

$$\delta(t) = 2\xi \sqrt{\alpha_v t} \,, \tag{29}$$

where ξ is obtained from the solution of the following transcendental equation:

$$\exp(\xi^2) \, \mathrm{erf}(\xi) \left[\xi - \frac{(T_\infty - T_{sat}) C_{p,v} k_l \sqrt{\alpha_v} \exp(-\xi^2 \frac{\rho_v^2 \alpha_v}{\rho_l^2 \alpha_l})}{h_{lv} k_v \sqrt{\pi \alpha_l} \, \mathrm{erfc}(\xi \frac{\rho_v \sqrt{\alpha_v}}{\rho_l \sqrt{\alpha_l}})} \right] = 0 \,, \tag{30}$$
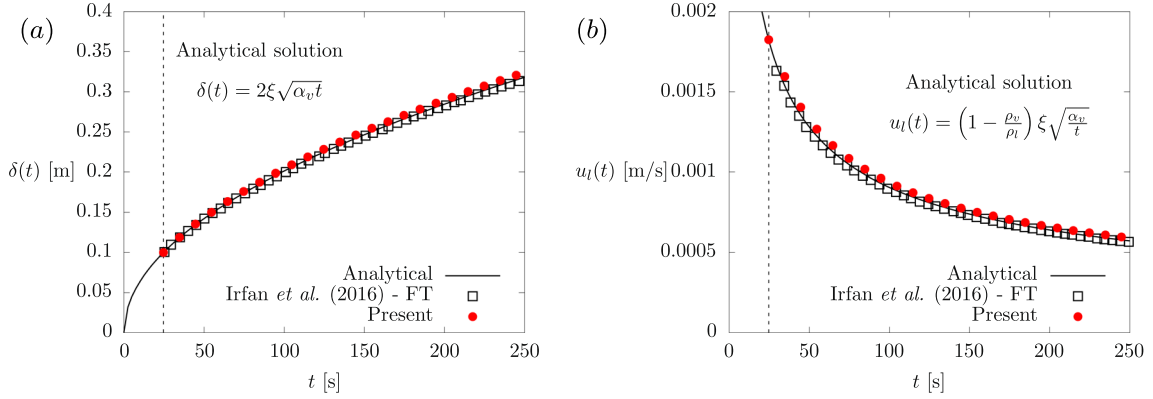
Fig. 7 Behavior of interface position (panel *a*) and liquid phase velocity (panel *b*) for the adsorption problem. The results are obtained using the same setup tested by Irfan and Muradoglu [23] using the front tracking (FT) method. Irfan and Muradoglu [23] results are shown using black empty squares. The simulation starts from the analytical profiles obtained for $t_0 = 24.7\ s$, which corresponds to an interface location equal to $\delta = 0.1\ m$ (vertical dashed line). The considered value of the vapor thermal diffusivity is $\alpha_v = 1.4 \times 10^{-3} m^2/s$ while the solution of the transcendental equation gives $\xi = 0.2689$

where α_i is the liquid/vapor thermal diffusivity and k_i is the liquid/vapor thermal conductivity. An analytical relation for the temperature in the liquid phase is also available:

$$T_l = T_\infty + \left[\frac{T_\infty - T_w}{\mathrm{erfc}(\xi \frac{\rho_v \sqrt{\alpha_v}}{\rho_l \sqrt{\alpha_l}})} \right] \mathrm{erfc}\left(\frac{x}{2\sqrt{\alpha_v t}} + \frac{\xi(\rho_v - \rho_l)}{\rho_l}\sqrt{\frac{\alpha_v}{\alpha_l}} \right), \tag{31}$$

while the vapor temperature is constant and uniform equal to $T_v = T_{sat}$. Finally, the velocity of the liquid phase can be obtained as:

$$u_l = \left(1 - \frac{\rho_v}{\rho_l} \right) \xi \sqrt{\frac{\alpha_v}{t}}, \tag{32}$$

We test the capabilities of the proposed method in reproducing this benchmark by considering two setups employed in archival literature. First, we reproduce the setup analyzed by Irfan and Muradoglu [23] using the front-tracking method. In particular, we consider a liquid and a vapor having a density equal to $\rho_l = 2.5\ kg/m^3$ and $\rho_v = 0.25\ kg/m^3$, corresponding to a density ratio of $\rho_v/\rho_l = 0.1$. The viscosities of the two phases are set equal to $\mu_l = 0.098\ kg/ms$ and $\mu_v = 0.007\ kg/ms$. The thermal conductivities are $k_v = 0.0035\ W/mK$ and $k_l = 0.0015\ W/mK$ while the specific heat at constant pressure is set equal to $C_{p,v} = C_{p,l} = 10\ J/kgK$. Finally, the latent heat has been chosen equal to $h_{lv} = 100\ J/kg$. The liquid is superheated with a temperature difference equal to $\Delta T = T_\infty - T_{sat} = 2\ K$. The simulation is performed using a domain having dimension $L_x = 1\ m$ and discretized with $N_x = 200$ grid points. For the phase-field method, we set $\epsilon = 1.5\Delta x$. For this setting, the resulting vapor thermal diffusivity is equal to $\alpha_v = 1.4 \times 10^{-3} m^2/s$ while the transcendental Eq. 30 gives $\xi = 0.2689$. The simulation starts from a time $t_0 = 24.7\ s$ so to avoid the singular condition obtained for $t = 0\ s$; the simulation then continues up to $t_f = 250\ s$. This initial time corresponds to an interface location equal to $x = 0.1\ m$.

The results obtained for the adsorption problem using the setup of Irfan and Muradoglu [23] are shown in Fig. 7. Panel *a* shows the interface position over time (red dots) while panel *b* shows the liquid velocity (red dots) over time. The analytical solutions, Eqs. (29)-(32), are reported using black continuous lines while the results obtained by Sun et al. [23] with black symbols. The initial simulation time, $t_0 = 24.7\ s$, is shown using a dashed vertical lines. We can observe that for both interface position and liquid velocity, present results (red circles) well match with the analytical results and archival literature data [23].

To further test the proposed method with a more challenging test case, we consider the setup analyzed by Irfan and Muradoglu [26]. Specifically, In the setting considered by Welch and Wilson [26], water properties at saturation conditions (standard pressure) are employed. The liquid and vapor densities are set equal to $\rho_l = 958.4\ kg/m^3$ and $\rho_v = 0.6\ kg/m^3$; the corresponding density ratio is $\rho_v/\rho_l = 6.2 \times 10^{-4}$. The viscosities of the two phases are $\mu_l = 2.8 \times 10^{-4}\ kg/ms$ and $\mu_v = 1.2 \times 10^{-5}\ kg/ms$, respectively. The liquid and vapor thermal conductivities are $k_l = 0.677\ W/mK$ and $k_v = 0.024\ W/mK$. Likewise, the specific
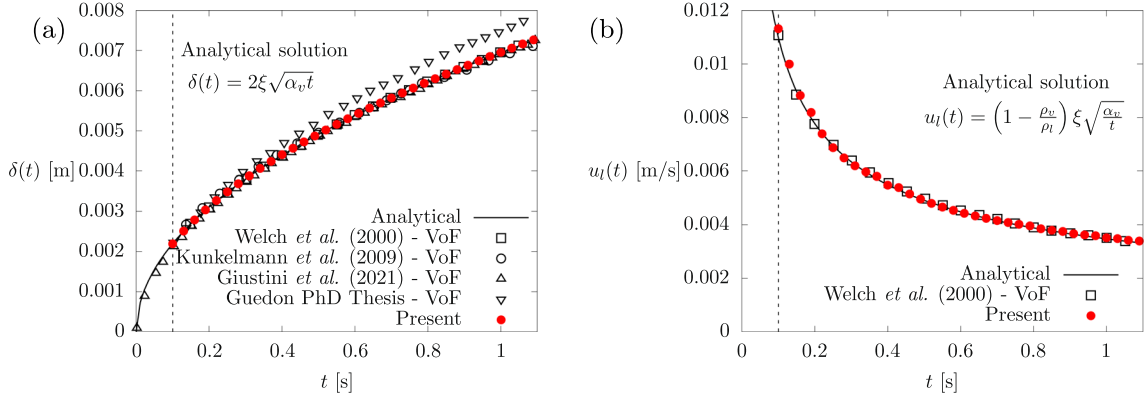
Fig. 8 Behavior of interface position (panel *a*) and liquid velocity (panel *b*) for the adsorption problem. The results refer to the setting employed by Welch and Wilson [26]. The simulation starts from the analytical profiles obtained for $t_0 = 0.1\ s$, which corresponds to an interface location equal to $\delta = 0.0022\ m$ (vertical dashed line). The vapor thermal diffusivity is $\alpha_v = 1.4 \times 10^{-3}\ m^2/s$ while the solution of the transcendental equation gives $\xi = 0.7763$. Present results (red circles) are compared against the analytical results (black lines) and archival literature data of Sun et al. [26] (empty squares), Kunkelmann and Stephan [64] (empty circles), Giustini and Issa [27] (empty upward triangles) and Guedon [62] (empty downward triangles). All archival literature results here reported have been obtained using a volume-of-fluid methodology

heat at constant pressure are set equal to $C_{p,v} = 2077\ J/kgK$ and $C_{p,l} = 4216\ J/kgK$. Finally, the latent heat is chosen equal to $h_{lv} = 2.25 \times 10^6\ J/kg$. The liquid is superheated with a temperature difference equal to $\Delta T = T_\infty - T_{sat} = 5\ K$. The domain has dimension $L_x = 0.1\ m$ and is discretized with $N_x = 200$ grid points. For the phase-field method, we set $\epsilon = 1.5\Delta x$. For this setting, the resulting vapor thermal diffusivity is $\alpha_v = 2.0 \times 10^{-5}\ m^2/s$ while the transcendental Eq. (30) gives $\xi = 0.7763$. The simulation starts from $t_0 = 0.1\ s$ and is continued up to $t_f = 1.1\ s$. This initial time corresponds to an interface location equal to $x = 0.0022\ m$.

The resulting interface position and liquid velocity are shown in Fig. 8, in panels *a* and *b*, respectively. Present results (red circles) are compared against the analytical results obtained from Eqs. (29)-(32), which are reported using black continuous lines. Archival literature results are also reported as reference: Welch and Wilson [26] (empty squares), Kunkelmann and Stephan [64] (empty circles), Giustini and Issa [27] (empty upward triangles) and Guedon [62] (empty downward triangles). We can notice that also for this setting, which employs water properties at saturation conditions (standard pressure), an excellent agreement is obtained among present results, analytical results and archival literature results for both interface position and liquid velocity.

3.4 Growth of a vapor bubble with a constant vaporization rate

In this final section, we test the method by considering the growth of a two-dimensional vapor bubble [27, 34,50,65,66]. We replicate here the setting proposed by Tanguy et al. [50]. In particular, we consider a vapor bubble having an initial radius equal to $R_0 = 0.001\ m$, located at the center of a squared domain, with a spatially uniform and temporally constant vaporization rate per unit surface $\dot{m} = 0.1\ kg/m^2\ s$, the bubble will grow for a time equal to $\Delta t = 0.01\ s$, until its radius is twice the initial one. The length and height of the computational domain are set equal to $L_x = L_y = 0.01\ m$. Outflow boundary conditions are imposed on the sides of the domain: pressure is imposed ($p = 0\ Pa$) while a zero normal derivative condition is imposed for the velocity ($\partial \mathbf{u}/\partial \mathbf{n} = 0$). A uniform grid spacing is used along the two directions. The liquid and vapor densities are set equal to $\rho_l = 1000\ kg/m^3$ and $\rho_v = 1\ kg/m^3$, corresponding to a density ratio of $\rho_v/\rho_l = 0.001$ and resembling water properties at saturation temperature and standard pressure conditions. The viscosities of the two phases are set equal to $\mu_l = \mu_v = 1 \times 10^{-3}\ kg/ms$. The surface tension is set equal to $\sigma = 0.07\ N/m$. As the vaporization rate per unit surface is constant and prescribed, no additional thermodynamical properties need to be defined, e.g. latent heat or specific heat. For the phase-field, we set $\epsilon = \Delta x$.

As the phase change rate is constant and uniform, the radius of the bubble will grow linearly over time:

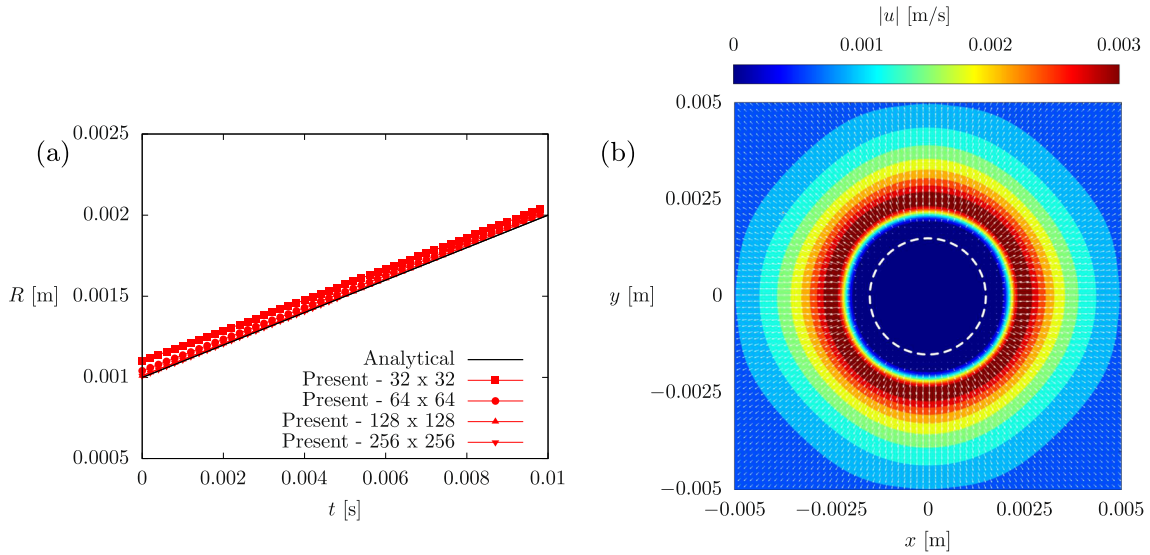$$R(t) = R_0 + \frac{\dot{m}}{\rho_v} t\ , \tag{33}$$

Fig. 9 Panel *a* shows the time evolution of the vapor bubble radius as a function of time. The analytical time evolution is reported with a thin black line while numerical results are shown with red symbols. Different grid resolutions have been tested: 32×32 (squares), 64×64 (circles), 128×128 (upward triangles) and 256×256 (downward triangles). Panel *b* shows a contour map of the velocity magnitude at $t = \Delta t/2 = 0.005 \ s$ using a grid resolution equal to 128×128. A white dashed line is used to identify the interface position (iso-contour $\phi = 0.5$). White arrows are used to identify the flow direction and magnitude

where R_0 is the initial bubble radius.

To assess the accuracy of the present method, we compare the theoretical evolution of the bubble radius (Eq. 33) against the numerical results. We test four different grid resolutions: 32×32, 64×64, 128×128 and 256×256. The results are shown in Fig. 9a. The theoretical behavior is reported with a thin black line while numerical results, which refer to different grid resolutions, are reported with red symbols: 32×32 (squares), 64×64 (circles), 128×128 (upward triangles) and 256×256 (downward triangles). We can observe that for all cases, the bubble growth is in good agreement with the analytical prediction. Specifically, by increasing the grid resolution, the agreement between numerical and analytical results improves and, for the largest grid resolution considered, the two lines perfectly overlap. Interestingly, we can observe that the overshot reported by Tanguy et al. [50] [Fig. 1] using the delta formulation (i.e. when a one-fluid approach is used to solve the Navier–Stokes equations in the entire domain, as in the present work) is here not observed. The reason for the better agreement between numerical and theoretical results obtained here can be traced back to the asymmetry of the phase-field profile and the smoothed velocity jump across the interface, as can be observed in Fig. 2a and also reported by Sun and Beckermann [37]. This avoids the generation of spurious currents with a magnitude similar to the induced velocity jump that can negatively affect the advection of the phase-field variable and thus the bubble growth. The asymmetry (or offset) of the phase-field profile and velocity jump can be appreciated qualitatively in Fig. 9b. Clearly, this offset becomes smaller as the capillary width is reduced. Panel *b* shows a contour map of the velocity magnitude (blue-low; red-high) while a white dashed line identifies the interface position (iso-contour $\phi = 0.5$). White arrows are used to show the velocity magnitude and its respective direction. The plot refers to the grid resolution 128×128. Looking at the qualitative figure, we can appreciate that the velocity jump (i.e. the transition from the zero velocity region located inside the vapor bubble and the non-zero velocity outside) is slightly offset compared to the interface location (white dashed line).

4 Conclusions

We propose a phase-field method for the description of boiling phenomena. The phase-field method, which relies on the conservative Allen–Cahn equation, is coupled with numerical solutions of the mass conservation and Navier–Stokes equations, used to describe the flow field, and energy equation, used to describe the temperature field. To close the set of governing equations, an energy-based model is used to compute the vaporization rate [49]. The proposed method is tailored towards large-scale simulations of phase-changing flows: i) For the interface description, the method employs a phase-field method that does not require any geometrical

reconstruction [42]; ii) For the flow-field description, the employed numerical discretization allows for the use of FFT-based direct solvers for the pressure Poisson equation.

The proposed approach is validated against different benchmarks: i) A flat interface that undergoes vaporization at a constant rate; ii) the Stefan problem, a flow instance in which a superheated vapor drives the vaporization of a liquid at saturation conditions; iii) The adsorption problem, a flow instance where a superheated liquid drives the vaporization of a vapor at saturation conditions; iv) The growth of a two-dimensional vapor bubble. For all the benchmarks, the proposed method exhibits an excellent agreement with analytical solutions and archival literature results for a wide range of density ratios, from $\rho_v/\rho_l = 1$ down to $\rho_v/\rho_l \simeq 5 \times 10^{-4}$. Future works will focus on more complex scenarios, as for instance film boiling and the parallelization and porting to GPUs of the proposed method.

Declarations

Conflict of interest All authors declare that they have no Conflict of interest.

References

1. Chen, Z., Wu, F., Utaka, Y.: Numerical simulation of thermal property effect of heat transfer plate on bubble growth with microlayer evaporation during nucleate pool boiling. Int. J. Heat Mass Transf. **118**, 989–996 (2018)
2. Silvi, L.D., Chandraker, D.K., Ghosh, S., Das, A.K.: Understanding dry-out mechanism in rod bundles of boiling water reactor. Int. J. Heat Mass Transf. **177**, 121534 (2021)
3. Leong, K.C., Ho, J.Y., Wong, K.K.: A critical review of pool and flow boiling heat transfer of dielectric fluids on enhanced surfaces. Appl. Therm. Eng. **112**, 999–1019 (2017)
4. Su, G.-Y., Wang, C., Zhang, L., Seong, J.H., Kommajosyula, R., Phillips, B., Bucci, M.: Investigation of flow boiling heat transfer and boiling crisis on a rough surface using infrared thermometry. Int. J. Heat Mass Transf. **160**, 120134 (2020)
5. Gallo, M., Magaletti, F., Cocco, D., Casciola, C.M.: Nucleation and growth dynamics of vapour bubbles. J. Fluid Mech. **883**, 14 (2020)
6. Gennari, G., Smith, E.R., Pringle, G.J., Magnini, M.: Coupled atomistic-continuum simulations of nucleate boiling. Int. J. Therm. Sci. **200**, 108954 (2024)
7. Kim, J.: Review of nucleate pool boiling bubble heat transfer mechanisms. Int. J. Multiph. Flow **35**(12), 1067–1076 (2009)
8. Chen, Y., Jin, S., Yu, B., Ling, K., Sun, D., Zhang, W., Jiao, K., Tao, W.: Modeling and study of microlayer effects on flow boiling in a mini-channel. Int. J. Heat Mass Transf. **208**, 124039 (2023)
9. Bures, L., Bucci, M., Sato, Y., Bucci, M.: A coarse grid approach for single bubble boiling simulations with the volume of fluid method. Comput. Fluids **271**, 106182 (2024)
10. Demou, A.D., Scapin, N., Pelanti, M., Brandt, L.: A pressure-based diffuse interface method for low-mach multiphase flows with mass transfer. J. Comput. Phys. **448**, 110730 (2022)
11. Kossolapov, A., Hughes, M.T., Phillips, B., Bucci, M.: Bubble departure and sliding in high-pressure flow boiling of water. J. Fluid Mech. **987**, 35 (2024)
12. Diemand, J., Angélil, R., Tanaka, K.K., Tanaka, H.: Direct simulations of homogeneous bubble nucleation: agreement with classical nucleation theory and no local hot spots. Phys. Rev. E **90**(5), 052407 (2014)
13. Shahmardi, A., Tammisola, O., Chinappi, M., Brandt, L.: Effects of surface nanostructure and wettability on pool boiling: a molecular dynamics study. Int. J. Therm. Sci. **167**, 106980 (2021)
14. Liu, H., Ahmad, S., Chen, J., Zhao, J.: Molecular dynamics study of the nanoscale boiling heat transfer process on nanostructured surfaces. Int. Commun. Heat Mass **119**, 104963 (2020)
15. Lavino, A.D., Smith, E., Magnini, M., Matar, O.K.: Surface topography effects on pool boiling via non-equilibrium molecular dynamics simulations. Langmuir **37**(18), 5731–5744 (2021)

16. Gallo, M., Magaletti, F., Casciola, C.M.: Thermally activated vapor bubble nucleation: the Landau-Lifshitz-Van der Waals approach. Phys. Rev. Fluids **3**(5), 053604 (2018)
17. Gallo, M., Casciola, C.M.: Vapor bubble nucleation in flowing liquids. Int. J. Multiph. Flow **179**, 104924 (2024)
18. Tryggvason, G., Scardovelli, R., Zaleski, S.: Direct Numerical Simulations of Gas–Liquid Multiphase Flows. Cambridge University Press, Cambridge (2011)
19. Mirjalili, S., Jain, S.S., Dodd, M.: Interface-capturing methods for two-phase flows: An overview and recent developments. Center for Turbulence Research Annual Research Briefs **2017**(117–135), 13 (2017)
20. Soligo, G., Roccon, A., Soldati, A.: Turbulent flows with drops and bubbles: what numerical simulations can tell us - freeman scholar lecture. ASME J. Fluids Eng. **143**, 080801–1 (2021)
21. Juric, D., Tryggvason, G.: Computations of boiling flows. Int. J. Multiph. Flow **24**(3), 387–410 (1998)
22. Esmaeeli, A., Tryggvason, G.: Computations of film boiling. Part I: numerical method. Int. J. Heat Mass Transf. **47**(25), 5451–5461 (2004)
23. Irfan, M., Muradoglu, M.: A front tracking method for direct numerical simulation of evaporation process in a multiphase system. J. Comput. Phys. **337**, 132–153 (2017)
24. Shin, S., Choi, B.: Numerical simulation of a rising bubble with phase change. Appl. Therm. Eng. **100**, 256–266 (2016)
25. Khorram, A., Mortazavi, S.: Direct numerical simulation of film boiling on a horizontal periodic surface in three dimensions using front tracking. Phys. Fluids **34**(5), 052117 (2022)
26. Welch, S.W., Wilson, J.: A volume of fluid based method for fluid flows with phase change. J. Comput. Phys. **160**(2), 662–682 (2000)
27. Giustini, G., Issa, R.I.: A method for simulating interfacial mass transfer on arbitrary meshes. Phys. Fluids **33**(8), 087102 (2021)
28. Son, G., Dhir, V.: Numerical simulation of film boiling near critical pressures with a level set method. J. Heat Transf. **120**(1), 183–192 (1998)
29. Gibou, F., Chen, L., Nguyen, D., Banerjee, S.: A level set based sharp interface method for the multiphase incompressible Navier–Stokes equations with phase change. J. Comput. Phys. **222**(2), 536–555 (2007)
30. Tanguy, S., Ménard, T., Berlemont, A.: A level set method for vaporizing two-phase flows. J. Comput. Phys. **221**(2), 837–853 (2007)
31. Shao, C., Luo, K., Chai, M., Wang, H., Fan, J.: A computational framework for interface-resolved DNS of simultaneous atomization, evaporation and combustion. J. Comput. Phys. **371**, 751–778 (2018)
32. Wang, Z., Zheng, X., Chryssostomidis, C., Karniadakis, G.E.: A phase-field method for boiling heat transfer. J. Comput. Phys. **435**, 110239 (2021)
33. Verdier, W., Kestener, P., Cartalade, A.: Performance portability of lattice Boltzmann methods for two-phase flows with phase change. Comput. Methods Appl. Mech. Eng. **370**, 113266 (2020)
34. Haghani-Hassan-Abadi, R., Fakhari, A., Rahimian, M.-H.: Phase-change modeling based on a novel conservative phase-field method. J. Comput. Phys. **432**, 110111 (2021)
35. Scapin, N., Shahmardi, A., Chan, W., Jain, S., Mirjalili, S., Pelanti, M., Brandt, L.: A mass-conserving pressure-based method for two-phase flows with phase change. In: Center for Turbulence Research Proceedings of the Summer Program (2022)
36. Tamura, A., Katono, K.: Development of a phase-field method for phase change simulations using a conservative Allen–Cahn equation. J. Nucl. Eng. **8**(3), 031402 (2022)
37. Sun, Y., Beckermann, C.: Diffuse interface modeling of two-phase flows based on averaging: mass and momentum equations. Physica D **198**(3–4), 281–308 (2004)
38. Chiu, P.-H., Lin, Y.-T.: A conservative phase field method for solving incompressible two-phase flows. J. Comput. Phys. **230**(1), 185–204 (2011)
39. Mirjalili, S., Ivey, C.B., Mani, A.: A conservative diffuse interface method for two-phase flows with provable boundedness properties. J. Comput. Phys. **401**, 109006 (2020)
40. Jain, S.S., Mani, A., Moin, P.: A conservative diffuse-interface method for compressible two-phase flows. J. Comput. Phys. **418**, 109606 (2020)
41. Safari, H., Rahimian, M.H., Krafczyk, M.: Extended lattice Boltzmann method for numerical simulation of thermal phase change in two-phase fluid flow. Phys. Rev. E **88**(1), 013304 (2013)
42. Roccon, A., Zonta, F., Soldati, A.: Phase-field modeling of complex interface dynamics in drop-laden turbulence. Phys. Rev. Fluids **8**, 090501 (2023)
43. Mirjalili, S., Mani, A.: Consistent, energy-conserving momentum transport for simulations of two-phase flows using the phase field equations. J. Comput. Phys. **426**, 109918 (2021)
44. Liu, H.-R., Ng, C.S., Chong, K.L., Lohse, D., Verzicco, R.: An efficient phase-field method for turbulent multiphase flows. J. Comput. Phys. **446**, 110659 (2021)
45. Mangani, F., Soligo, G., Roccon, A., Soldati, A.: Influence of density and viscosity on deformation, breakage, and coalescence of bubbles in turbulence. Phys. Rev. Fluids **7**, 053601 (2022)
46. Mirjalili, S., Khanwale, M.A., Mani, A.: Assessment of an energy-based surface tension model for simulation of two-phase flows using second-order phase field methods. J. Comput. Phys. **474**, 111795 (2023)
47. Brown, L., Jain, S., Moin, P.: A phase field model for simulating the freezing of supercooled liquid droplets. Technical report, SAE Technical Paper (2023)
48. Mohammadi-Shad, M., Lee, T.: Phase-field lattice Boltzmann modeling of boiling using a sharp-interface energy solver. Phys. Rev. E **96**(1), 013306 (2017)
49. Kharangate, C.R., Mudawar, I.: Review of computational studies on boiling and condensation. Int. J. Heat Mass Transf. **108**, 1164–1196 (2017)
50. Tanguy, S., Sagan, M., Lalanne, B., Couderc, F., Colin, C.: Benchmarks and numerical methods for the simulation of boiling flows. J. Comput. Phys. **264**, 1–22 (2014)
51. Schrage, R.W.: A theoretical study of interphase mass transfer. Columbia University Press, New York (1953)

52. Carey, V.P.: Liquid-vapor Phase-change Phenomena: an Introduction to the Thermophysics of Vaporization and Condensation Processes in Heat Transfer Equipment. CRC Press, Boca Raton (2020)
53. Tanasawa, I.: Advances in condensation heat transfer **21**, 55–139 (1991)
54. Hardt, S., Wondra, F.: Evaporation model for interfacial flows based on a continuum-field representation of the source terms. J. Comput. Phys. **227**(11), 5871–5895 (2008)
55. Magnini, M., Pulvirenti, B., Thome, J.R.: Numerical investigation of hydrodynamics and heat transfer of elongated bubbles during flow boiling in a microchannel. Int. J. Heat Mass Transf. **59**, 451–471 (2013)
56. Jafari, R., Okutucu-Özyurt, T.: Phase-field modeling of vapor bubble growth in a microchannel. J. Comput. multiph. Flows **7**(3), 143–158 (2015)
57. Udaykumar, H.S., Shyy, W., Rao, M.M.: Elafint: a mixed Eulerian–Lagrangian method for fluid flows with complex and moving boundaries. Int. J. Numer. Methods Fluids **22**(8), 691–712 (1996)
58. Jain, S.S.: Accurate conservative phase-field method for simulation of two-phase flows. J. Comput. Phys. **469**, 111529 (2022)
59. Chorin, A.J.: Numerical solution of the Navier–Stokes equations. Math. Comput. **19**, 745–762 (1968)
60. Sun, D., Xu, J., Chen, Q.: Modeling of the evaporation and condensation phase-change problems with fluent. Numer. Heat Transf. B: Fundam. **66**(4), 326–342 (2014)
61. Carslaw, H., Jaeger, J.: Conduction of heat in solids. Clarendon, Oxford (1959)
62. Guedon, G.R.: Two-phase heat and mass transfer modeling: flexible numerical methods for energy engineering analyses (2013)
63. Rajkotwala, A., Panda, A., Peters, E., Baltussen, M., Geld, C., Kuerten, J., Kuipers, J.: A critical comparison of smooth and sharp interface methods for phase transition. Int. J. Multiph. Flow **120**, 103093 (2019)
64. Kunkelmann, C., Stephan, P.: CFD simulation of boiling flows using the volume-of-fluid method within openfoam. Numer. Heat Transf. A **56**(8), 631–646 (2009)
65. Zheng, X., Babaee, H., Dong, S., Chryssostomidis, C., Sakis, G.E.: A phase-field method for 3D simulation of two-phase heat transfer. Int. J. Multiph. Flow **82**, 282–298 (2015)
66. Malan, L., Malan, A.G., Zaleski, S., Rousseau, P.: A geometric VOF method for interface resolved phase change and conservative thermal energy advection. J. Comput. Phys. **426**, 109920 (2021)